EES Solar

PAPER

View Article Online
View Journal | View Issue

Cite this: *EES Sol.*, 2025, **1**, 89

Extracting contact recombination from FFT-filtered photoluminescence imaging of half-metallised silicon solar cells†

Yifu Shi,[a] David N. R. Payne,[b] Andreas Fell,[cf] Cyril Leon,[c] Tim Niewelt,[cd] Edris Khorani,[d] Peter R. Wilshaw,[a] John D. Murphy,[d] Kuninori Okamoto[e] and Ruy S. Bonilla *[a]

In high-performance Si solar cells, recombination at the metal-silicon interface has become the major remaining barrier to reaching the theoretical power conversion efficiency limit. Efficient and practical assessment of metal-associated recombination is crucial for understanding and mitigating these losses. This study presents a photoluminescence imaging-based method for evaluating the metal contact recombination current ($J_{0,c}$) of rear TOPCon metallisation. The proposed method is based on the Fourier analysis of the periodic pattern corresponding to the metal fingers on samples. This requires no specially designed metallisation geometries. Noise normalisation and bandpass filtering in k-space are used to suppress noise and preserve the metal contrast signal. Numerical device simulations are used to establish the relation between contact recombination levels and the resulting metal contrasts in photoluminescence images. Testing this technique using data from samples made with two different metallisation pastes demonstrates the differences in contact recombination $J_{0,c}$ values, showing the practical application of the technique. Experimental conditions, including PL illumination and camera resolution, are discussed to determine their influence on the efficacy of the proposed method. This Fourier analysis-based $J_{0,c}$ determination method is well-suited for industrial finger grid metallisation and has the potential to enable seamless contact characterisation for PV manufacturing.

Received 8th October 2024
Accepted 20th January 2025

DOI: 10.1039/d4el00016a

rsc.li/EESSolar

Broader context

Solar energy plays a vital role in the global transition to sustainable and renewable energy, with silicon photovoltaic technology leading as the most cost-effective and widely adopted solution. As the world increases renewable energy capacity, improving the efficiency and scalability of silicon PV technology becomes increasingly critical. Recombination loss at metal contact interfaces is a major limiting factor in high-efficiency silicon PV devices. Rapid, accurate, and integrated methods are required to characterise the energy losses at metal contacts. Our study introduces an innovative method for evaluating contact recombination losses in silicon solar cells using Fourier transform filtering and physical modelling of photoluminescence images. Unlike existing methods that rely on specially designed metallization patterns, our technique leverages the periodicity of industrial screen-printed metal patterns to extract contact recombination without modifying industrial processes. The extraction of metal-specific luminescence signals marks a significant advancement, allowing for accurately determining losses in practical manufacturing environments. By providing a scalable and efficient characterisation solution, our method supports the broader aim of reducing costs and enhancing the performance of silicon photovoltaics, contributing to the global shift towards renewable energy.

1 Introduction

In the recent evolution of crystalline silicon (c-Si) photovoltaic technologies, increases in cell efficiency have primarily been driven by advances in contact passivation. Passivated contact architectures, such as the tunnelling oxide passivated contacts (TOPCon)[1] and silicon heterojunction (SHJ)[2] have pushed c-Si cells closer to the Shockley–Quiesser theoretical power conversion efficiency (PCE) limit. By effectively alleviating minority carrier recombination losses in the contacting regions, such technologies enabled very low energy losses in contacts with low resistivity. The recombination parameter J_0, denoting the dark recombination current density, is a widely used standard for

[a]*Department of Materials, University of Oxford, Oxford, OX1 3PH, UK. E-mail: sebastian.bonilla@materials.ox.ac.uk*
[b]*School of Engineering, Macquarie University, NSW 2109, Australia*
[c]*Fraunhofer Institute for Solar Energy Systems ISE, Freiburg, 79110, Germany*
[d]*School of Engineering, University of Warwick, Coventry, CV4 7AL, UK*
[e]*Changzhou Fusion New Material Co Ltd, Changzhou, 213031, China*
[f]*AF Simulations GmbH, March, 79232, Germany*

† Electronic supplementary information (ESI) available: Extended figures on the PL intensity for the baseline recombination of TOPCon cells, including the breakdown of recombination as a function of illumination. All Python, PC3D, and Quokka files are made available *via* ORA or our online repository: **https://github.com/OxfordInterfacesLab**. See DOI: **https://doi.org/10.1039/d4el00016a**

assessing recombination processes in both experiments and modelling.[3] J_0 can be used as the cumulative global parameter in device dark saturation current or specifically for surface recombination processes as a surface parameter.[4] Furthermore, to differentiate between recombination from the contacted and non-contacted surface regions, contact-related $J_{0,c}$ is explicitly used for the recombination at the metal-silicon interface. $J_{0,c}$ is therefore established and widely adopted as an important characterisation metric in evaluating contact performance in Si solar cells.[5,6]

In industrial settings, c-Si solar cell metallisation predominantly relies on a flatbed screen printing and fast firing process using Ag-based metallisation pastes.[7] Such a fire-through metallisation route, partly historically inherited from older lines, can be adapted to contacting poly-Si passivated TOPCon-like surfaces with only minor modifications to the paste.[8,9] However, studies on poly-Si based contacts have identified a trade-off: reducing the thickness of the poly-Si layer decreases parasitic losses but, in turn, increases the susceptibility to metal paste ingress during the firing process. This susceptibility leads to large-area removal of SiN_x and poly-Si layers under contacts, accompanied by Ag metal intrusion into the substrate. Such microstructures are linked to excessive contact-induced recombination losses.[8,10] Early experimentally extracted $J_{0,c}$ values for fire-through metallisation on various n^+ poly-Si films range from 100–400 fA cm^{-2}.[10,11] More recent studies show that $J_{0,c}$ values below 50 fA cm^{-2} are achievable on thin n^+ poly (~100 nm) structures through precise tuning of the poly-Si deposition[12] or doping process.[13]

Photoluminescence imaging (PLI) is a rapid and versatile characterisation tool in PV applications.[14] PLI operates on the principle that photoluminescence intensity depends on the fraction of excess carriers undergoing radiative recombination. This allows quantitative analyses of luminescence emission intensities to assess carrier recombination processes, including contact recombination, $J_{0,c}$. In earlier studies, recombination at contacts ($J_{0,c}$) was treated as part of the area-weighed total J_0 in a linear fitting of J_0 to metal-area coverage fraction.[15] Developments in simulation tools such as Quokka and Griddler facilitate more accurate $J_{0,c}$ determination by enabling the calculation of lateral non-uniform carrier density distribution. Accounting for carrier non-uniformity has improved the interpretation of PL intensity in test fields with known metallisation fractions, thereby enhancing the accuracy of $J_{0,c}$ fitting.[6,16,17] Recent works have also revealed variations in $J_{0,c}$ as a function of the spatial locations and variations with metallisation dimensions.[18,19]

One major limitation of the approaches that use test fields is that they require a specially printed metallisation pattern with sub-regions of varying metallised fractions. This prevents the method from being applied in regular production line metrology. This work is based on using Fourier analysis to extract $J_{0,c}$ from the PLI spatial pattern without requiring a variety of metal coverages, as originally suggested by Saint-Cast *et al.*[20,21] The Fourier analysis exploits the spatial periodicity in the luminescence yield to assess metal recombination under periodic metal fingers. Saint-Cast *et al.*[20,21] converts PLI into spatial V_{oc} maps by calibration with a contacted voltage measurement. Their work used an analytical model to calculate an estimated average PL intensity and an oscillation amplitude based on a pair of iV_{oc} and emitter contact $J_{0,c}$. Experimental data from PL can hence be compared to the model outputs to determine theoretical iV_{oc} and $J_{0,c}$ values. Their work later focused on complete solar cells with both-side metallisation. During PLI there are contacts on the imaging side, with a major challenge being that some of the periodicity in luminescence originated simply from the contact shading. Our work uses a modified approach where single-side metallised samples are PL imaged with the non-contacted surface facing the PL camera. Notably, such samples are still easier to produce compared to test fields required by other methods, *i.e.* simply omitting the screen-printing step on one side. Since we then can use total luminescence yield from the non-metallised side, our set-up does not suffer from finger shading artefacts. As it has been shown for other methods that the 2D carrier distribution profile affects accurate J_{0c} extraction,[18] we extend the previously proposed Fourier method by replacing the 1D analytical model with 2D numerical device simulations. This increases overall accuracy by avoiding errors from model simplifications, and also makes the method generally applicable to any device configuration, *e.g.* front or rear emitter location. Furthermore, K-space filtering is implemented in our work to enhance the detection of the periodic metal contrast signal, meaning low $J_{0,c}$ results <50 fA cm^{-2} can be extracted.

In this study, the samples examined feature standard industrially printed and fired metal contacts on a TOPCon rear passivation structure. We use both PC3D[22] and Quokka3 (ref. 23) for rapid simulation of the spatial distribution of excess carrier densities and photoluminescence emission patterns resulting from metal-related recombination. Quokka3 additionally accounts for the impact of reabsorption in combination with optical filtering to increase accuracy. The spatial periodicity in PLI data is used to isolate and quantify $J_{0,c}$ from the contrast extracted after Fast Fourier Transform (FFT) bandpass filtering and noise rejection. We demonstrate that $J_{0,c}$ can be extracted by fitting experimentally measured metal contrasts to simulation results with the aid of the Fourier analysis procedure. We further discuss experimental parameters that impact the efficacy of this method.

2 Sample structure and PL characterisation

Fig. 1(a) depicts the sample structure with an AlO_x passivated diffused boron emitter front and a poly-Si (150 nm) on oxide (TOPCon) rear, both capped with a silicon nitride surface passivation layer. The samples are 210 × 210 mm TOPCon wafers fabricated in 2021 with busbar-less line Ag paste metallisation only on the TOPCon rear side. The metallisation was fabricated using the mainstream screen printing and belt-furnace firing process. We compared two groups of samples with differences in the metal paste compositions, referred to as paste A and paste B. Each group included 9 samples. Paste B has

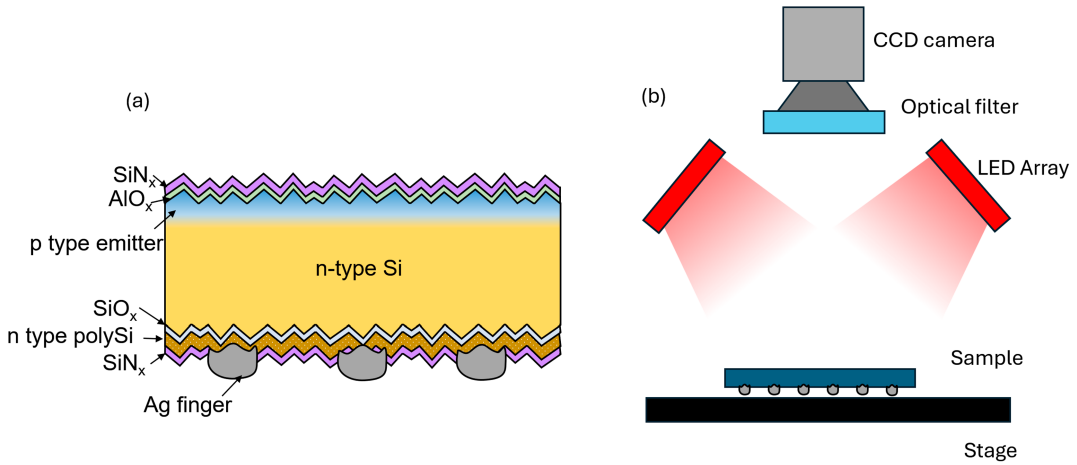

Fig. 1 (a) The half-metallised TOPCon sample structure. (b) Schematic of the PL setup, the sample has the metal side facing down.

a reduced glass frit composition, designed to reduce the etching depth during firing.

Room temperature photoluminescence images were captured using a PL Imaging tool with 650 nm LED array as outlined in Fig. 1(b). The silicon CCD camera used was an Apogee AltaF with a Kodak KAF-3200ME sensor, which has a resolution of 2184 × 1472 pixels. Samples were placed on a low reflectivity black stage (to minimise back reflection) with the metallised TOPCon side facing down and the non-metalized emitter side facing up. A consistent integration time of 12 seconds was used for all images. To reduce the impact of camera sensor noise, five images were acquired and averaged for each sample. Images were taken at an illumination intensity equivalent to 1-sun intensity, except when otherwise indicated in illumination tests.

Fig. 2(a) demonstrates the front view of the full metallisation grid pattern on a wafer. A finger width of 30 μm and a finger pitch of 1.5 mm were measured with optical microscopy. Fig. 2(b) shows an example PL image from the region indicated by the square in Fig. 2(a). This image covers a total of 112 rear metal fingers running vertically from left to right. Among various other dark defects, the rear metal recombination pattern can be observed as repeating darker stripes in this image since it produces enhanced recombination.

Recombination at the rear metal interfaces reduces local excess carrier densities. Therefore, a luminescence intensity contrast exists between the metal-contacted, high recombination region, and the non-contacted surfaces away from it. Such a contrast correlates with the excess metal recombination $J_{0,c} > J_{0,\mathrm{TOPCon}}$ at the rear, where $J_{0,\mathrm{TOPCon}}$ indicates the recombination current density of the rear non-contacted surface. However, considering the rough spatial sampling in our PLI setup – 78 μm per camera pixel size, the direct extraction of PL contrast between metallised/unmetallised regions can be inaccurate. Additionally, as seen in Fig. 2(b), pronounced PLI non-uniformities can mask the periodic contrast from the metallisation pattern. Such dark patches arise from sample handling, with some visible wafer features, including segregation rings and edge recombination.

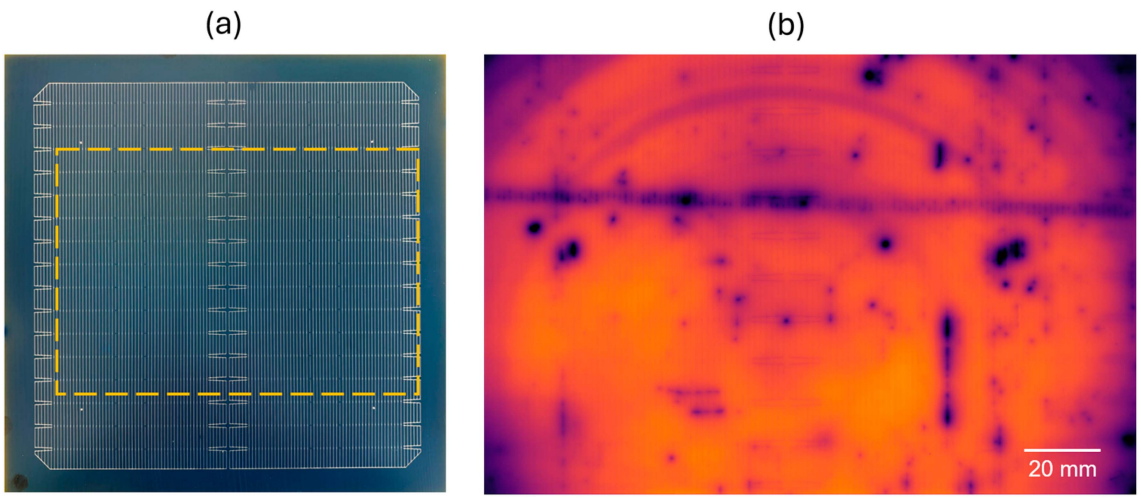

Fig. 2 (a) Metallisation grid pattern on a 210 × 210 mm wafer, (b) PL image example taken with metallisation at rear.

Fortunately, the metal-induced pattern in PL images is 1D periodic in nature, which means the signal has a known repetition rate in the horizontal direction. This provides the basis for employing Fourier analysis. By transforming PL data into the frequency domain, Fourier analysis allows for isolation of the periodic signal corresponding to the metallisation pattern, enabling noise filtering and enhancing the detection of such a specific metal-recombination-related contrast.

3 Fast Fourier transform and filtering

The analysis method presented in this work is based on the mathematical Fourier transform. For digital signals with a finite length, the relevant Discrete Fourier Transform (DFT) in one dimension (1D) is formulated in eqn (1). This process converts a series x_n on spatial x-domain to a complex-valued series X_k in the (spatial) frequency k-domain. The inverse IDFT process, shown in eqn (2), converts the k-domain representation back to x-domain. The computationally efficient Fast Fourier Transform (FFT) algorithm for computing DFT is used for fast data processing, available in tools such as the Python package SciPy.

The DFT and IDFT are given by:

$$\text{DFT}: \quad X_k = \sum_{n=0}^{N-1} x_n e^{-i2\pi \frac{k}{N} n} \tag{1}$$

$$\text{IDFT}: \quad x_n = \frac{1}{N} \sum_{k=0}^{N-1} X_k e^{i2\pi \frac{n}{N} k} \tag{2}$$

where X_k is the k-th element of the frequency domain series, x_n is the n-th element of the space domain series, N is the total sample number, and i is the imaginary unit.

The process of Fourier analysis and filtering applied to an experimental measured PL image is illustrated in Fig. 3(a–d):

(a) Fig. 3(a) shows an example of normalised PL luminescence x_n along a horizontal line as a function of distance for just one line of the PL image. Luminescence intensity counts at each pixel of the line are normalised to the line average value to examine any variations on a relative scale. Notable features of the line profile include long-range variations as well as the pixel-by-pixel camera noise (as seen in the inset zoom-in plot). These noises are over-imposed to the periodic metal line contrast signal and hence need to be deconvoluted.

(b) Fig. 3(b) presents the k-domain spectrum of the normalised line profile after FFT. The y-axis gives the complex modulus of the converted Fourier series X_k. The x-axis gives the symmetrical half of frequencies ranging from 0 to sampling rate/2. The initial high value at zero-frequency X_0, indicated by the yellow arrow, is the numerical sum of the series.

When a periodic signal is operated by FFT, a series of peaks appear at the fundamental frequency and its harmonics (multiples). The green arrows indicate the locations for the first 3 harmonics of the metallisation spatial frequency of ~0.66 mm^{-1} (1/spacing). As weaker peaks at higher $n \geq 2$ harmonics can be lost to the noise floor, only the first peak is examined, which is marked by the dashed circle in Fig. 3(b).

(c) Fig. 3(c) shows a zoom-in view of the spectrum around the marked first harmonic peak in Fig. 3(b). The broadband noise floor level here is significant, only positioned at 1.5 (on a logarithmic scale with base e) below the peak value. Such noise in the k-domain results from spatial domain noise, including camera sensor noise and wafer spatial defects.

A band-selective filter window (green) is chosen to isolate the signal at the 0.66 mm^{-1} frequency, the metallisation repetition rate. It is possible to define the width of the band-pass filter, here set to be 0.04. The average noise level is obtained from two normalisation windows (yellow) adjacent to the main window. The noise level is first subtracted from the FFT signal, and then

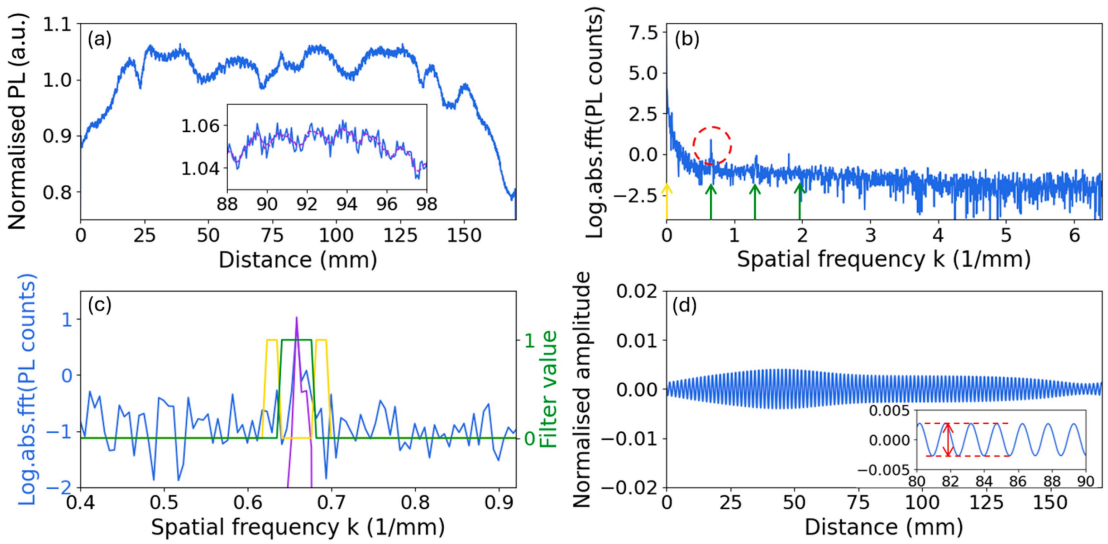

Fig. 3 (a) Original PL counts in x-domain along a line profile in the horizontal image direction, with inset showing noised-covered periodicity. (b) FFT-transformed line profile in k-domain. (c) A zoom-in in k-domain towards the peak at fundamental metal line frequency, with filter windows displayed as overlays. (d) Reconstructed signal and with inset showing wave amplitude.

the green filter window (rectangular cut-off bandpass filter) is applied to eliminate components at all other frequencies. The resulting noise-subtracted, FFT-filtered signal is shown in purple.

(d) Fig. 3(d) illustrates the wave reconstructed from the filtered signal by inverse FFT. This band-pass filtered wave appears enveloped because of the rectangular windowing process. The information of interest in Fig. 3(d) is the amplitude of the oscillatory variation, which is used to calculate the metal-induced PL periodic contrast, given by:

$$\text{Metal contrast}: \quad C_{\text{metal}} = \frac{A_{\text{ave}}}{S_{\text{ave}}} \times 100\%$$

A_{ave} is the average amplitude of oscillations in the reconstructed signal. It represents the average of individual oscillation amplitudes, where each amplitude is determined by the difference between the neighboring maximum and minimum, as highlighted in red in the inset of Fig. 3(d). S_{ave} denotes the average signal level of the line profile, which has the value of one 1 in this case since the PL signal has been normalised. The percentage metal contrast C_{metal} is defined as such as a key figure of merit in our characterisation, representing the metal-induced average variation in PL profiles.

The metal contrast of the full image can be obtained as the average of the results from all horizontal lines. Only 1D FFT is needed because the periodicity only exists in the horizontal direction. Such a process applies to all PL sample images provided they have the same metal grid pattern. In a production line, all solar cells can hence be analysed against the same periodicity.

4 Numerical simulation for PL metal contrast

To establish the link between the metal recombination parameter $J_{0,c}$ and the abovementioned PL metal contrast, quantitative modelling of the spatial carrier distribution and luminescence emission profile with $J_{0,c}$ as an input parameter is required. Instead of using an analytical model as in previous works, we employ 2D numerical device simulations, which increases the model accuracy by considering also the depth-dependence of the carrier distribution. We use both PC3D[22] and Quokka3,[23] which are silicon solar cell simulation programs capable of solving drift-diffusion carrier transport in (up to) three dimensions. They implement the conductive boundary model where surface layers, including the thin emitter at the front, are treated optically and electronically as boundary conditions for the bulk. Consequently, quasi-neutrality can be assumed in the bulk to solve the carrier drift-diffusion differential equations efficiently.[24,25] Both tools implement a similar analytical optical model based on lumped internal optical parameters of the surfaces.[22,26] Notably, in Quokka3, the same optical model can also be used to simulate the reabsorption of emitted photons, which, in combination with the consideration of spectral sensitivity of the luminescence detection setup, increases the accuracy of the predicted spatial PL profiles. If not stated otherwise, the results shown in the following are produced by PC3D.

Fig. 4(a) shows the sample cross-section under PL measurement with metallisation on the rear. The red dashed square marks the 2D simulation unit cell, spanning half the area between two fingers. Fig. 4(b) illustrates the dimensions of the unit cell and the boundary conditions for cell simulation. The left and right edges of the unit cell are symmetrical boundaries. The recombination levels at surface boundaries are defined by front surface recombination $J_{0,\text{front}}$, rear TOPCon surface recombination $J_{0,\text{TOPCon}}$ and rear metal contact recombination $J_{0,c}$. The numerical device simulation requires a full set of parameters in addition to the surface recombination conditions. These include wafer electrical and optical properties, surface and bulk recombination parameters, and illumination conditions. Table 1 lists the key parameters in use for setting up

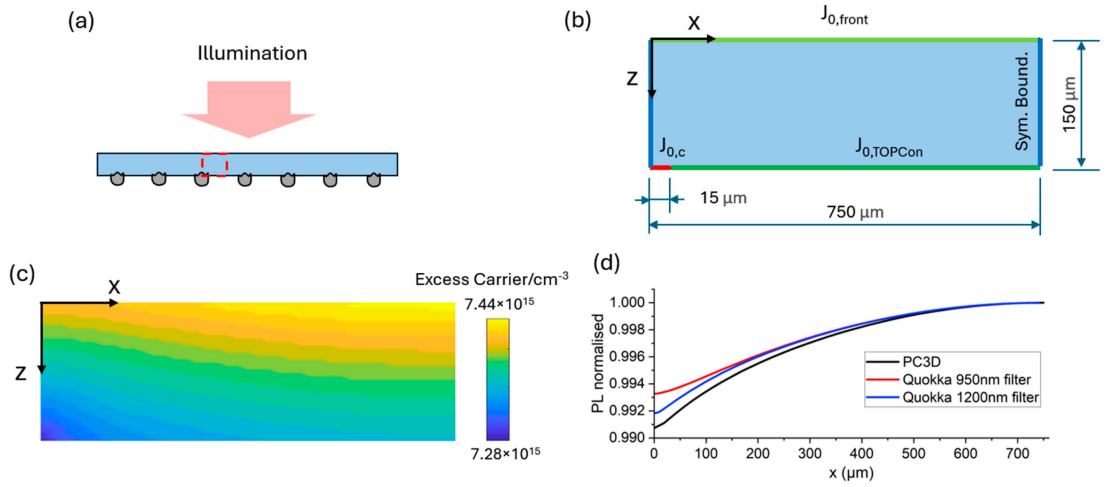

Fig. 4 (a) Sample with simulation unit cell marked. (b) Boundaries of the unit cell bulk with dimensions. (c) Excess carrier population 2D map in unit cell solved my PC3D for PL test conditions. (d) Normalised PL line profile of the unit cell, comparing the PC3D result with additional Quokka3 results for two different short-pass filtering assumptions.

Table 1 Device parameters defined in PC3D simulation

Device information	**n-type base doping** 4.00×10^{-15} cm^{-3}	**Resistivity** 1.21 Ω cm	**Thickness** 150 μm
Bulk recombination	**Bulk SRH τ_{n0}** 0.5 ms	**Bulk SRH τ_{p0}** 5 ms	**Auger recombination coefficient** 8.3×10^{-31} cm^6 s^{-1}
Surface recombination	**Front J_{01} ($J_{0,front}$)** 25 fA cm^{-2}	**Rear J_{01} ($J_{0,TOPcon}$)** 5–100 fA cm^{-2} (10 fA cm^{-2} in Fig. 4(c))	**Rear metal ($J_{0,c}$)** 5–140 fA cm^{-2} (50 fA cm^{-2} in Fig. 4(c))
Illumination condition	**Type** Monochromatic	**Wavelength** 650 nm	**Generation current density** 48.8 mA cm^{-2}

the simulation. Surface recombination properties are determined to match the experimentally measured full-cell performance parameters (V_{oc},J_{sc} and FF) obtained from complete cells that underwent the same processing route, with the only addition being the printed front silver contacts.

Fig. 4(c) presents the excess carrier population map solution within the unit cell domain under such parameter inputs. It can be observed that the steady-state excess carrier density distribution under 650 nm illumination is spatially well homogenised across the wafer bulk due to the high diffusion length, with total variation confined in a small range: $(7.28–7.44) \times 10^{15}$ cm^{-3}. Meanwhile, the excess recombination at the metal boundary ($J_{0,c} > J_{0,TOPCon}$) acts as a sink for excess carriers, resulting in a local low concentration and inducing gradients (steady-state currents) towards the metal.

The PL emission profile along the horizontal x-direction is computed from the 2D carrier profile by integrating the radiative recombination multiplied with an escape probability term over the depth z, see example in.[27] Such a model is built in Quokka3, while for the case of PC3D we use a simplified approach as given in eqn (3):

$$\text{PL emission}: \quad \text{PL}_x = \int_{z=0}^{D} \Delta n_{x,z}(\Delta n_{x,z} + n_0) \times B_{\text{rad}} \times \exp(-\alpha z)\mathrm{d}z \tag{3}$$

where $\Delta n_{x,z}$ is the excess carrier density at location (x, z), n_0 is the equilibrium concentration, B_{rad} is the radiative recombination coefficient, and α is the photon absorption coefficient for the monochromatic 1150 nm wavelength representative for the actual emission spectrum. The first two terms describe the emission rate from band-to-band recombination. The final exponential term accounts for reabsorption of emission from depths z within the wafer. The value of exponential term remains close to 1 here within depths of concern because of the low absorption at $\alpha = 6.8 \times 10^{-5}$ μm^{-1}, which points to negligible attenuation by reabsorption at 1150 nm. We stress that this formulation is a strongly simplified model of detected PL intensity. A hyperspectral comprehensive expression of detected luminescence signal includes three parts: a spectral emission function, an escape probability function related to sample internal optics, and an additional detection sensitivity term for the PL camera.[28,29] Such approach is implemented in Quokka3, which we use to showcase the impact of using a short-pass filter in the luminescence detection setup. A short-pass filter of 950 nm or 1200 nm cut-off wavelength is often added to the standard high-pass filter that rejects visible stray light in the PL camera. The purpose of the short-pass filter is to provide a smaller window of detectivity in the camera CCD, which sharpens the image since only photons emitted near the surface of the Si specimen are detected. We perform Quokka simulations with a perfect 950 nm and 1200 nm short-pass filter, representing the two extremes of very aggressive and essentially no short-pass filtering.

Exemplary simulated PL profiles are shown in Fig. 4(d). The difference between PC3D and Quokka3 results are dominated by two effects: (i) more simplistic silicon material models are used in PC3D, in particular band-gap-narrowing is not considered, which becomes relevant also in the bulk for such high V_{oc} samples; (ii) more simplistic luminescence emission model used for the PC3D results. It can be shown that PC3D results with the simple single 1150 nm wavelength luminescence emission model yield results very close to Quokka3, assuming no short-pass filtering, when ensuring the same Si material properties in both tools. Notably, the Quokka3 results in Fig. 4(d) show a significant influence of the short-pass filter on the PL profile. This motivates proper luminescence modelling, which includes the spectral sensitivity of the optical detection system for increased accuracy of the presented method. Also note that the luminescence modelling in either case does not consider lateral optical blurring, which is another source of error. This is typically addressed by using a suitable short-pass filter to only detect the wavelengths less prone to blurring. Short-pass filtering and its consideration in the simulations is therefore of particular importance for this method's accuracy.

5 Linking PL contrast to metal recombination

Fig. 5(a) illustrates the PL intensity obtained from the device simulations, where the effect of the metallisation-induced excess recombination is evident on the unit cell PL intensity profile. Here, the rear TOPCon surface recombination current density $J_{0,TOPCon}$ is kept at 10 fA cm^{-2}, which provides the baseline against which the excess metal recombination $J_{0,c}$–$J_{0,TOPCon}$ is measured. The plots in Fig. 5(a) are PL intensity profiles normalised to the max value furthest away from metal, *i.e.* at the middle between two metal fingers. This series demonstrates the increasing variation amplitude of PL profiles with increasing excess contact recombination, given by $J_{0,c}$–$J_{0,TOPCon}$.

To simulate a full line signal containing 112 metal fingers, the unit cell profile is mirrored and concatenated 112 times.

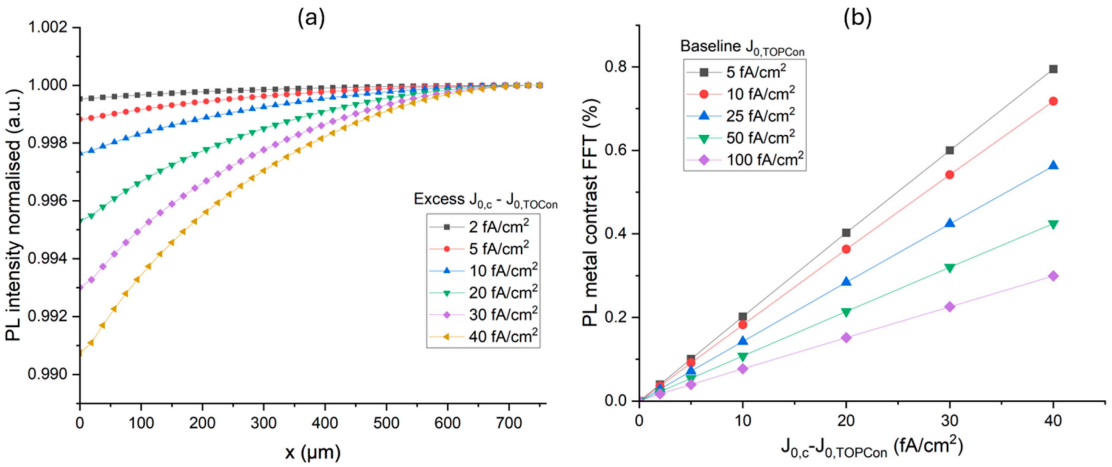

Fig. 5 (a) Normalised PL intensity line profile series in the unit cell, with a $J_{0,TOPCon} = 10$ fA cm^{-2}, and varying excess $J_{0,c}$–$J_{0,TOPCon}$ (b) PL metal contrasts extracted by FFT *vs.* excess $J_{0,c}$–$J_{0,TOPCon}$.

The same Fourier analysis process applied to the experimentally measured image lines is used for the simulated lines, allowing for the extraction of metal contrast values following the same route. The red curve in Fig. 5(b) depicts metal contrasts as a function of excess $J_{0,c}$–$J_{0,TOPCon}$ for a baseline $J_{0,TOPCon}$ of 10 fA cm^{-2}. The relation is nearly linear within the $J_{0,c}$–$J_{0,TOPCon} = 0$–40 fA cm^{-2} range, with a Pearson's correlation coefficient $\rho = 0.99998$. This points to a simple correlation between contrast and excess metal recombination.

The rest of the curves in Fig. 5(b) represent different baseline $J_{0,TOPCon}$ conditions. Comparison of these curves reveals that higher baseline surface recombination levels reduce the contrast from metal recombination. This is intuitively evident since the worse the recombination of the free surface, the less difference between the carrier densities under the contact and under the non-contacted region. Hence it is important to establish the baseline $J_{0,TOPCon}$ before contrast calibration, as it impacts the correlation between contrast and excess metal recombination in our methodology. In the ESI (Fig. S1),† we show that the overall average PL intensity from PC3D simulation has a strong dependency on TOPCon baseline surface recombination $J_{0,TOPCon}$. On the other hand, the average PL intensity is minimally influenced by the excess $J_{0,c}$ within the $J_{0,c}$ range of our concern (Fig. S1†). Therefore the $J_{0,TOPCon}$ of individual samples can be correlated to their average image luminance. Following this, the relationships between metal contrast to the excess $J_{0,c}$–$J_{0,TOPCon}$ can be interpolated from Fig. 5(b) for individual samples based on their baseline $J_{0,TOPCon}$ values. Such relationships are then used to estimate the $J_{0,c}$–$J_{0,TOPCon}$, and therefore $J_{0,c}$, for each half-metalized sample in this study.

Fig. 6(a) presents the estimated baseline $J_{0,TOPCon}$ and $J_{0,c}$ values for the two experimental groups. The two groups share same pre-metallisation surface passivation, with an all-sample average $J_{0,TOPCon}$ of 10 fA cm^{-2}. The error bars of the J_0

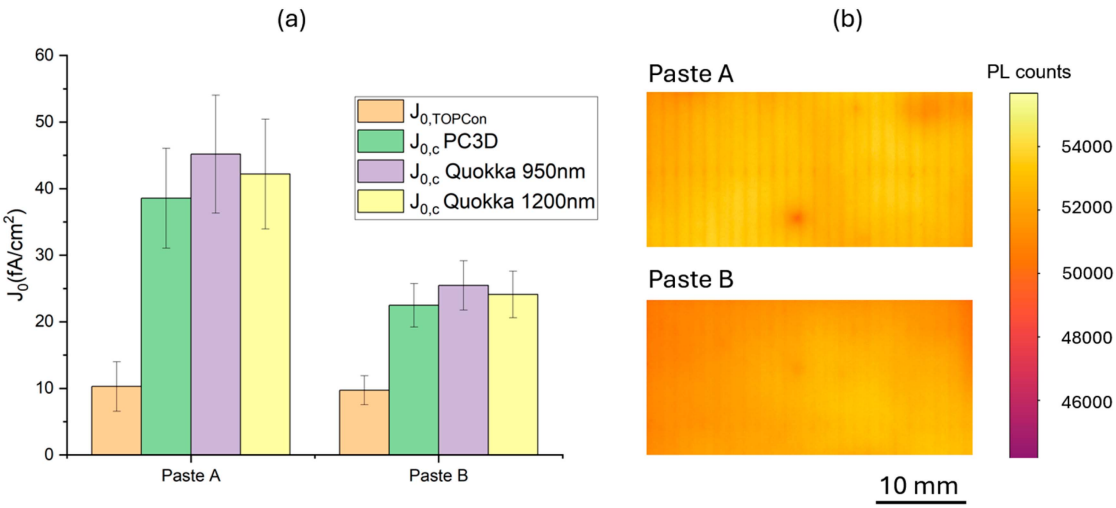

Fig. 6 (a) Estimated baseline $J_{0,TOPCon}$ values, and $J_{0,c}$ values extracted using both PC3D and Quokka for metal paste A and B. (b) PL image examples from a paste A sample a paste B sample, on same colour scale, enlarged to demonstrate the difference in metal line contrast.

numbers indicate the standard deviation among the 9 sample values within each group. The results confirm that, while both groups share a similar baseline $J_{0,\mathrm{TOPCon}}$ values, the samples in the paste B group have significantly lower $J_{0,c}$ values at 22 fA cm^{-2} when compared to the paste A group at 38 fA cm^{-2}. Additionally, enlarged original PL images from a paste A and a paste B sample are shown on the same colour scale in Fig. 6(b). It becomes evident from the comparison that the metal contrast from paste B is weaker than paste A, which gives rise to the difference in $J_{0,c}$ results. This finding underscores the efficacy of paste B's design in minimising surface damage during firing. Also included in Fig. 6(a) are the results using Quokka3 with different short-pass filter assumptions, as explained above. Quokka3 results are considered overall more accurate due to more detailed silicon material models, and highlight again the impact of considering short-pass filtering within the simulations.

For ease of application, PC3D and Quokka3 simulation files and python scripts for Fourier interpretation of simulation results and PL images are attached in ESI.† Similar contrast *vs.* $J_{0,c}$ relations can be obtained for customised samples. We recommend caution in determining/assigning the non-contacted surface recombination value ($J_{0,\mathrm{TOPCon}}$) because of its high relevance to the final contrast.

6 Discussion

Effective implementation of our $J_{0,c}$ analysis method relies on the accurate extraction of the metal contrast from the peak in *k*-space. Under the image acquisition conditions used here, featuring a high noise floor, peak extraction is prone to losses when the metal line contrast is weak due to low signal-to-noise ratios or small excess $J_{0,c}$. This issue can undermine the effectiveness of our noise filtering process and compromise the certainty in contrast quantification. Due to the necessity for a clear signal peak at *k*-space above noise floor, or equivalently, a high metal contrast, it is useful to identify the experimental parameters that may enhance the measured metal contrasts.

We first examined the relationship between varying illumination intensities and metal contrast. Experimental data points for one representative wafer sample are given as the red symbols plotted in Fig. 7(a). This data indicates a trend that metal contrast increases with illumination intensity. Complementing such an observation, PC3D simulations were conducted for an illumination intensity sweep, showing metal contrasts from FFT analysis at varying illumination intensities. The simulations, illustrated as the line traces in Fig. 7(a), show the contrast *vs.* illumination relation under different $J_{0,c}$ scenarios (with the same baseline $J_{0,\mathrm{TOPCon}} = 10$ fA cm^{-2}). The simulation results corroborate the experimental trend that higher illuminations lead to enhanced metal contrasts under all metal recombination scenarios. Therefore, higher illumination is helpful in improving signal clarity for such Fourier analysis method.

This trend can be linked to the injection dependence of lifetime observed on the samples. Surface recombination can become an increasingly important component limiting lifetime under higher injection conditions. The PC3D breakdown of total recombination in ESI Fig. S2† shows that, for an exemplar setting with a rear $J_{0,\mathrm{TOPCon}} = 50$ fA cm^{-2} and $J_{0,c} = 10$ fA cm^{-2}, the proportion of rear surface recombination increases from 25% to 28%, at illumination ranging from 0.05 suns to 2 suns. In such cases, using higher illumination levels enhances the prominence of rear surface metal features ($J_{0,c} > J_{0,\mathrm{TOPCon}}$) in the spatial distribution of carrier density, thus improving the detectability of such features.

It is also evident in Fig. 7(a) that the changes in measured metal contrast under different illumination conditions do not align completely with the simulated trends with fixed $J_{0,c}$ conditions. This discrepancy may arise from potential changes in $J_{0,c}$ across different injection levels. It can also arise from variations in the noise level in PL images captured under

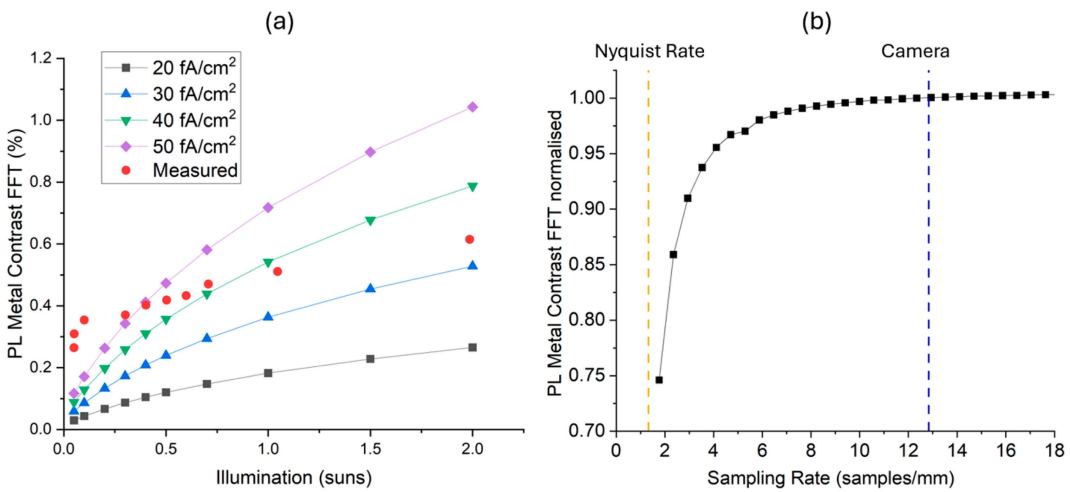

Fig. 7 (a) Metal contrast extracted *via* FFT under a range of illumination conditions, curve series show different metal recombination scenarios. (b) Normalised metal contrast extracted *via* FFT *vs.* sampling rate.

varying illumination. The high noise level, especially in low illumination images, can impact the effectiveness of the FFT signal filtering process. Such results suggest the limited applicability of the current method under different illumination conditions, indicating the need for further investigation in future work.

Additionally, we explored the impact of camera resolution on metal contrast. The camera resolution in the horizontal direction (the long detector axis) determines sampling rate of the line profile, which dictates the sampling interval both in *x*-space and *k*-space. To evaluate the effect of sampling rates, we used a range of sampling intervals (corresponding to the sampling rate from 2 to 18 mm^{-1}) to sample a near-continuous PC3D generated full line profile. We then carried out the FFT analysis following the same *k*-space filtering procedure on the sampled signal. Fig. 7(b) shows resulting metal contrast plotted as a function of sampling rate given in mm^{-1}. The contrast on the *y*-axis is shown as normalised values to the contrast at a standard sampling rate of 12.8 mm^{-1}, which is a close match to the operational camera rate (indicated by a blue line) with a horizontal resolution of 2184 pixels. The theoretical minimum Nyquist rate for sampling the metal pattern with 112 fingers is marked by an orange line. Loss of information can occur with inadequate sampling as shown on the left half of the curve. The curve also shows that while the contrast sharply increases above the Nyquist low limit, it plateaus at higher sampling rates, indicating minimal gains beyond the current sampling rate. This relationship reveals the sampling requirement for effective assessment of metal contrast.

7 Conclusions

In this work, we have demonstrated an effective and versatile method for extracting contact recombination $J_{0,c}$ from photoluminescence images of single-side metallised TOPCon wafer samples, without the need for specially designed metallisation geometries. The key to this method is exploiting the periodicity of the metal grid for isolation of the metal contrast signal in the *k*-space after performing Fast Fourier Transformation (FFT). Noise normalisation and filtering can be implemented as part of the Fourier analysis process, vastly enhancing the ability to extract information out of in-line PV manufacturing metrology. Numerical device simulations are used for modelling 2D carrier profiles and corresponding PL intensity profiles within a local unit cell. Interpretation of full-line simulation results *via* the Fourier analysis procedure demonstrates a linear-like relation of $J_{0,c}$ and PL metal contrast. The relationship is employed to estimate $J_{0,c}$ from images gathered from sample sets fabricated using two different metal pastes. The results demonstrate that using this method, TOPCon metallisation $J_{0,c}$ levels as low as 22 fA cm^{-2} can be extracted, indicating potential applicability on up-to-date passivated contact structures. Specifically, $J_{0,c}$ values of 38 fA cm^{-2} and 22 fA cm^{-2} were found for the two sample sets based on the assumption of a $J_{0,TOPCon}$ of 10 fA cm^{-2}, showing a reduction of metal recombination with the modified paste B composition. We highlight the influence of short-pass filtering, which should be included in the simulations for increased accuracy. Furthermore, the impact of illumination intensity and camera resolution on measurable metal contrast was investigated. We show that increasing illumination and camera sampling rate are beneficial to the efficacy of the Fourier analysis process. The insights of this work can benefit both PL imaging analysis and characterisation of contacts, both of which are key tools for the further optimisation of future solar cell designs.

Data availability

All data created during this research and published in this article is openly available from the Oxford University Research Archive and can be downloaded free of charge from **http://ora.ox.ac.uk**.

Conflicts of interest

There are no conflicts to declare.

Acknowledgements

Y. S. would like to acknowledge funding from China Scholarship Council – University of Oxford Scholarship for supporting his PhD studies (award number: 20196880044). R. S. B is supported by the Royal Academy of Engineering under the Research Fellowship scheme (RF\201819\18\38). This work is supported by the Engineering and Physical Sciences Research Council (EPSRC) grant numbers EP/V038605/1, EP/J01768X/2, and EP/V037749/1, the University of Oxford John Fell Fund, and a Leverhulme Trust Research Project Grant (RPG-2020-377). A. Fell and C. Leon acknowledge support by the German Federal Ministry for Economic Affairs and Climate Action within the project "KISS-PV" (03EE1129A). Metallisation samples were provided by Changzhou Fusion New Materials Co Ltd. For the purpose of Open Access, the author has applied a CC BY NC public copyright license to any Author Accepted Manuscript (AAM) version arising from this submission.

References

1 S. W. Glunz, B. Steinhauser, J. I. Polzin, C. Luderer, B. Grübel, T. Niewelt, A. M. O. M. Okasha, M. Bories, H. Nagel, K. Krieg, F. Feldmann, A. Richter, M. Bivour and M. Hermle, *Prog. Photovoltaics Res. Appl.*, 2021, **31**, 341–359.
2 Z. Sun, X. Chen, Y. He, J. Li, J. Wang, H. Yan and Y. Zhang, *Adv. Energy Mater.*, 2022, **12**, 2200015.
3 A. Cuevas, *Energy Procedia*, 2014, **55**, 53–62.
4 K. R. McIntosh and L. E. Black, *J. Appl. Phys.*, 2014, **116**, 014503.
5 A. Edler, V. D. Mihailetchi, L. J. Koduvelikulathu, C. Comparotto, R. Kopecek and R. Harney, *Prog. Photovoltaics Res. Appl.*, 2015, **23**, 620–627.
6 M. Li, J. Wong, N. Chen, A. G. Aberle and R. Stangl, *IEEE J. Photovolt.*, 2018, **8**, 1470–1477.
7 S. Tepner and A. Lorenz, *Prog. Photovoltaics Res. Appl.*, 2023, **31**, 557–590.

8 P. Padhamnath, J. Wong, B. Nagarajan, J. K. Buatis, L. M. Ortega, N. Nandakumar, A. Khanna, V. Shanmugam and S. Duttagupta, *Sol. Energy Mater. Sol. Cells*, 2019, **192**, 109–116.
9 P. Padhamnath, A. Khanna, N. Balaji, V. Shanmugam, N. Nandakumar, D. Wang, Q. Sun, M. Huang, S. Huang, B. Fan, B. Ding, A. G. Aberle and S. Duttagupta, *Sol. Energy Mater. Sol. Cells*, 2020, **218**, 110751.
10 H. E. Çiftpinar, M. K. Stodolny, Y. Wu, G. J. M. Janssen, J. Löffler, J. Schmitz, M. Lenes, J. M. Luchies and L. J. Geerligs, *Energy Procedia*, 2017, **124**, 851–861.
11 M. K. Stodolny, J. Anker, B. L. J. Geerligs, G. J. M. Janssen, B. W. H. Van De Loo, J. Melskens, R. Santbergen, O. Isabella, J. Schmitz, M. Lenes, J. M. Luchies, W. M. M. Kessels and I. Romijn, *Energy Procedia*, 2017, **124**, 635–642.
12 N. Nandakumar, J. Rodriguez, T. Kluge, T. Groβe, L. Fondop, P. Padhamnath, N. Balaji, M. König and S. Duttagupta, *Prog. Photovoltaics Res. Appl.*, 2019, **27**, 107–112.
13 P. Padhamnath, A. Khanna, N. Nandakumar, N. Nampalli, V. Shanmugam, A. G. Aberle and S. Duttagupta, *Sol. Energy Mater. Sol. Cells*, 2020, **207**, 110358.
14 T. Trupke, B. Mitchell, J. W. Weber, W. McMillan, R. A. Bardos and R. Kroeze, *Energy Procedia*, 2012, **15**, 135–146.
15 M. Fırat, H. Sivaramakrishnan Radhakrishnan, S. Singh, F. Duerinckx, M. Recamán Payo, L. Tous and J. Poortmans, *Sol. Energy Mater. Sol. Cells*, 2022, **240**, 111692.
16 D. Herrmann, S. Lohmuller, H. Hoffler, A. Fell, A. A. Brand and A. Wolf, *IEEE J. Photovolt.*, 2019, **9**, 1759–1767.
17 A. Fell, D. Walter, S. Kluska, E. Franklin and K. Weber, *Energy Procedia*, 2013, **38**, 22–31.
18 D. Herrmann, D. R. C. Falconi, S. Lohmuller, D. Ourinson, A. Fell, H. Hoffler, A. A. Brand and A. Wolf, *IEEE J. Photovolt.*, 2021, **11**, 174–184.
19 M. Li, N. Iqbal, Z. Yang, X. Lin, N. K. Pannaci, C. Avalos, T. Shaw, T. Jurca and K. Davis, *IEEE J. Photovolt.*, 2020, **10**, 1277–1282.
20 C. Leon, P. Saint-Cast, A. Fell, J. M. Greulich and S. Rein, *Sol. RRL*, 2023, **7**, 2300539.
21 P. Saint-Cast, D. Herrmann and H. Hoffler, *IEEE J. Photovolt.*, 2020, **10**, 554–559.
22 P. A. Basore, *PC3D* [Online] **http://www.pc3d.info**.
23 A. Fell, J. Schön, M. C. Schubert and S. W. Glunz, *Sol. Energy Mater. Sol. Cells*, 2017, **173**, 128–133.
24 P. A. Basore, *IEEE J. Photovolt.*, 2020, **10**, 905–911.
25 A. Fell, *IEEE Trans. Electron Devices*, 2013, **60**, 733–738.
26 A. Fell, J. Greulich, F. Feldmann, C. Messmer, J. Schön, M. Bivour, M. C. Schubert and S. W. Glunz, *Sol. Energy Mater. Sol. Cells*, 2022, **236**, 111534.
27 C. Schinke, D. Hinken, J. Schmidt, K. Bothe and R. Brendel, *IEEE J. Photovolt.*, 2013, **3**, 1038–1052.
28 A. Fell, T. Niewelt, B. Steinhauser, F. D. Heinz, M. C. Schubert and S. W. Glunz, *Sol. Energy Mater. Sol. Cells*, 2021, **230**, 111198.
29 C. Schinke, D. Hinken, J. Schmidt, K. Bothe and R. Brendel, *IEEE J. Photovolt.*, 2013, **3**, 1038–1052.